This article has been accepted for publication in a future issue of this journal, but has not been fully edited. Content may change prior to final publication. Citation information: DOI 10.1109/TUFFC.2019.2927439, IEEE Transactions on Ultrasonics, Ferroelectrics, and Frequency Control

Grain scattering noise modelling and its use in the detection and characterisation of defects using ultrasonic arrays

Long Bai, Alexander Velichko, and Bruce W. Drinkwater

***Abstract*—In the field of ultrasonic array imaging for non-destructive testing (NDT), material structural noise caused by grain scattering is one of the main sources of error when characterising defects that are found in polycrystalline materials. The existence of grains can also severely affect the detection performance of ultrasonic testing, making small defects indistinguishable from the grain indications due to ultrasonic attenuation and backscatter. This paper proposes a model in which the statistical distribution of the defect data is obtained from different realisations of the grain structure. This statistical distribution, termed the defect+grains model in this paper, is shown to contain information that is needed for detection and characterisation of defects. Hence, given a specific measurement configuration, the characterisation result can be obtained by constructing a defect+grains model based on multiple realisations of each possible defect and calculating their probability. The detection, classification, and sizing accuracy are shown to be predictable by quantifying the probabilities that an experimentally measured defect matches the different defect+grains models. This defect+grains modelling approach gives insight into the detection/characterisation problem, leading to an evaluation of the fundamental limits of the achievable inspection performance.**

I. Introduction

ULTRASONIC inspection is a widely used technique in NDT [1], [2]. An important application can be found for inspection of nuclear power plants, where ultrasound is often considered to be preferable to radiography due to the safety concerns related to the use of X-rays [3]. In recent years, the capability of using ultrasound to detect and characterise defects has improved significantly with the introduction of transducer arrays and advanced imaging algorithms, such as the total focusing method (TFM) [4], the inverse wave field extrapolation (IWEX) method [5], and the wavenumber algorithm [6]. The 6dB drop approach [7] is the industry standard for sizing defect using ultrasonic NDT based on scanned single-element data or array images. Although the use of higher frequencies and shear waves (*e.g.* combined with a deconvolution approach [8]) can help to improve the time resolution of ultrasonic A-scans, the achievable imaging resolution, and hence the sizing performance, is well known to be limited by diffraction. In practice this means that only defects larger than about two wavelengths can be reliably sized [9].

The authors are with the Department of Mechanical Engineering, University of Bristol, Bristol, UK (e-mail: lb13340@bristol.ac.uk).

Besides the difficulty in characterising small defects, another main challenge which limits the application of image-based inspection in the nuclear industry is caused by the existence of grains in polycrystalline materials [10]. Ultrasonic attenuation and backscatter caused by the interaction of the ultrasonic waves with the grains can severely affect the SNR of the measured signals and resultant images. High-frequency inspection and/or materials with large grains are particularly challenging because attenuation increases with the grain size and frequency for grain sizes of practical interest [11]. For example, in the Rayleigh regime (*i.e.* grain size is much smaller than the wavelength), the attenuation coefficient is proportional to the fourth power of the frequency and the third power of the grain size [11], suggesting that low-frequency inspection should be used in order to detect small defects [12]. Low frequencies are, however, undesirable for defect characterisation because of the poor imaging resolution. The grains also cause the backscattered echoes to be contaminated with coherent noise [13], which was shown to significantly degrade the performance of super-resolution imaging algorithms for defects in a copper sample [14].

Signal processing algorithms were previously shown to offer the potential to reduce the amount of grain noise seen in an image. Newhouse *et al.* introduced the split spectrum processing (SSP) technique [15] which decomposes the wide-band spectrum of a received signal into a number of sub-bands. The defect signal is coherent over these sub-bands while the grain noise is expected to be incoherent. As a result, the grain noise can be suppressed by non-linearly recombining the spectra from these sub-bands. Matz *et al.* proposed a de-noising procedure based on a wavelet filtering approach [16]. In a separate study which aimed to suppress grain noise within time of flight diffraction (TOFD) A-scan signals measured from austenitic stainless steel welds, Praveen *et al.* showed that higher order wavelets with large number of filter coefficients could result in higher SNRs compared to lower order wavelets [17]. Other filtering approaches, including the use of an adaptive least mean square error filter [18] and a time-frequency Wiener filter [19], were also reported for grain noise cancellation. Unlike the aforementioned work which adopted general-purpose filters as the de-noising tool, the multiple scattering filter (MSF) is a more recent approach which was specifically designed to address the detection problem in a highly scattering medium [20]. The MSF was used in combination with a time-reversal imaging algorithm DORT [21] for improved detection of 2mm side-drilled holes in an Inconel

This article has been accepted for publication in a future issue of this journal, but has not been fully edited. Content may change prior to final publication. Citation information: DOI 10.1109/TUFFC.2019.2927439, IEEE Transactions on Ultrasonics, Ferroelectrics, and Frequency Control

600 block at depths of 50mm and 70mm [22]. However, sizing of the small side-drilled holes remained difficult due to the poor imaging resolution. A high resolution Bayesian imaging approach was also proposed [23] and applied to detection and localisation of small defects in the presence of multiple scattering. The only defect parameter considered was scattering cross-section, which if used alone, could not provide sufficient information for defect characterisation.

Because grain scattering introduces coherent noise to the measurement, it is difficult to completely remove grain noise without also removing part of the defect signal using filtering approaches. Although it offers the potential to facilitate improved imaging/detection of defects in certain cases, the change in amplitude and shape of the defect signal due to filtering can potentially make defect characterisation (*e.g.* sizing of defects based on the scattering amplitude [9]) unreliable. The filtering approaches also require a detection threshold to determine the existence of a defect signal [16], [20]. Although the threshold plays an important role in de-noising (and hence, detection) performance, its selection is somewhat arbitrary (*e.g.* small defects may become detectable using low threshold values, but this also results in high false alarm rates) [24]. More importantly, these filtering approaches have the fundamental limitation that they do not provide insight into the detection/characterisation problem as well as how the characterisation uncertainty can be evaluated given some measurement.

Faced with issues related with imaging and filtering approaches discussed above, we consider using the frequency-domain scattering matrix [9] for detection and characterisation of defects in this paper. The scattering matrix consists of the far-field scattering coefficients of a defect for incident and scattering angles measurable from a given configuration, and is known to encode all the information about the defect geometry [25]. Hence, it is an ideal choice of input feature for any inversion approach aiming at retrieving defect parameters (*e.g.* length and width) from the array measurements [26]. In practice, the time-domain array data is superposition of responses from many defects that are close to each other, and an additional procedure (*e.g.* the sub-array imaging [27] and inverse imaging [28] approaches) can be applied to suppress the interference from other defects when extracting the scattering matrix of the target defect.

Previous work on defect characterisation generally falls within one of the following two categories. The first type of approaches aim to reconstruct the defect shape based on the integral representation of the scattered wave field in terms of the wave field at the boundary of a defect [29]. The defect shape can be obtained by adopting global optimisation approaches (*e.g.* the simulated annealing algorithm [30]) or through the use of non-iterative inversion schemes (*e.g.* the linear sampling method [31]). The second type of approaches, which are "more targeted", characterise defects by extracting a few critical defect parameters based on the understanding that there are a limited number of possible defect types which can realistically occur in a component [25]. The second approach is adopted in this paper, and more specifically, we use the scattering matrix to evaluate the influence of the grain scattering noise on detection and characterisation. The main purpose of this paper is as follows. Firstly, the statistics of the defect and noise scattering matrices in noisy materials are explored based on repeated forward simulations. This statistical information is then used in an inversion framework based on Bayes theorem [25] to explore the performance of defect characterisation and sizing. In addition, uncertainty in detection/characterisation is shown to arise from the overlapping between the probability density functions of two or more defect (or noise) data distributions. The achievable inspection performance can be evaluated by quantifying this overlap, and this quantitative information is useful as the cost function in a range of optimisation problems in ultrasonic NDT (*i.e.* transducer array optimisation and selection of wave modes).

II. Forward modelling

A. Grain scattering modelling

Understanding and modelling the grain scattering noise in polycrystalline materials is important for detection and characterisation purposes [32], and it has been studied by many researchers in the fields of ultrasonic NDT and power generation industry [32], [33], [34], [35]. In this paper, we focus our attention on the use of two-dimensional, elastic, finite element (FE) modelling [36] of the sample including the defects and the grains. This approach naturally captures all the physical phenomena relevant to ultrasonic wave propagations in polycrystalline metallic elastic media and was previously shown to be accurate when compared to experimental data [32]. The main advantage of this method is that it offers the flexibility in modelling different materials, grain sizes and defects. With the finite element method, we can quickly explore many such realisations (this paper contains 350 such realisations, from which 1750 defect and noise scattering matrices are extracted). Hence the finite element model is the key to enabling us to make the progress we describe. A random grain structure can be obtained with the use of Voronoi diagrams [37], and below is a brief description of the approach adopted in this paper. More details about the forward modelling procedure, including FE modelling of 3D structures, can be found in [34]. Also, it is worth pointing out that the grain parameters (*e.g.* the mean grain size) and defect sizes/types considered in this paper can readily be modified (or extended) to model specific applications in the future.

The first step in simulating a grain structure is to create uniform grid points within the sample. The grid points are then shifted by a random amount that follows a Gaussian distribution. The spacing of the initial grid points determines the average grain size (*i.e.* grain diameter), and the standard deviation of the Gaussian distribution (termed the shift parameter hereafter) is linked to the grain size variation of the final structure. A Voronoi diagram is created based on these randomly distributed grid points (nodes), and Fig. 1(a) shows an example of the Voronoi diagram in a 5mm×5mm region. As can be seen, the Voronoi diagram divides the sample region into a number of convex polygons, each containing one node and defining the region of the diagram that is closest to the node [12]. To model a quasi-isotropic material such

This article has been accepted for publication in a future issue of this journal, but has not been fully edited. Content may change prior to final publication. Citation information: DOI 10.1109/TUFFC.2019.2927439, IEEE Transactions on Ultrasonics, Ferroelectrics, and Frequency Control

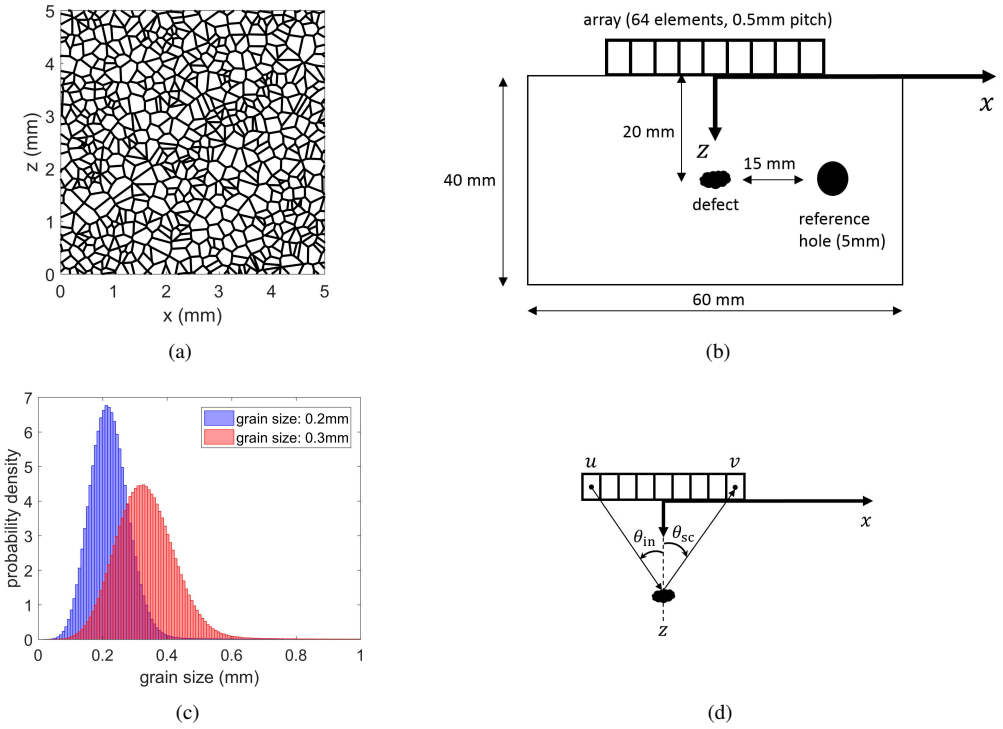

Fig. 1. (a) An example grain structure (the mean grain size and the shift parameters are 0.2mm and 0.4mm), (b) measurement configuration used for simulating the array data, (c) grain size distribution of the simulated samples, and (d) notation used for imaging and defining the scattering matrix. In (d), an incident angle θ_{in} (or a scattering angle θ_{sc}) is positive if it is measured clockwise from the z-axis. The target defect in (b) and (d) is modelled to be cracks or holes of sizes 1-3mm in this paper, and it can be of any type or size in practice.

as Type 304 stainless steel, each grain is assumed to have a random orientation in 3D (however, for 2D FE modelling in this paper, the rotated stiffness matrix is reduced from 3D to 2D under the plane strain assumption [34].) We note that Type 304 stainless steel is commonly used in pressure vessels in the nuclear power industry and assume the material parameters $c_{11} = 2.16 \times 10^{11}\text{N/m}^2$, $c_{12} = 1.45 \times 10^{11}\text{N/m}^2$, $c_{44} = 1.29 \times 10^{11}\text{N/m}^2$, and $\rho = 7860\text{kg/m}^3$ (c_{11}, c_{12}, and c_{44} are elastic constants of a cubic material) [38], [39].

Figure 1(b) shows the measurement configuration adopted in this paper. The overall approach uses a linear system model [40] in which the electronics and transducer characteristics lead to a particular input signal. This signal is then used in an FE model and received signals are similarly processed. As can be seen from Fig. 1(b), a 64 element linear array with an element pitch of 0.5mm is used on a sample with the depth of 40mm. The excitation signal is chosen to be a wideband input signal with a centre frequency of 2.5 MHz. Hence, the received signal is also wide-band (although containing less high frequency contents due to attenuation), which enables us to extract defect (and grain noise) data and compare imaging/characterisation results at different frequencies. In this paper, imaging and scattering matrix extraction are performed for frequencies between 1 MHz and 3 MHz, and the array is always Nyquist spatially-sampled within this frequency range. The target defect is located at a distance of 20mm from the surface, and it is aligned with the array centre. A 5mm side-drilled hole is introduced on the right-hand-side of the defect as a reference scatterer (see Section IV-A). As explained in Section I, multiple measurement data for a given defect are needed to calculate the statistics of the defect+grains model. The array data are simulated from different realisations of the grain structure, with Pogo [41] being used as the FE solver. Pogo has the advantage of utilising the computational power of graphics processing units (GPUs) and is reported to reduce the processing time by up to 200 times compared to a CPU-based commercial software [41]. A regular mesh is used in FE for computational efficiency, and the grain boundaries are modified to match the meshes in FE. The element size of 80μm is used for the configuration shown in Fig. 1(b), and this corresponds to 23 elements per wavelength at the highest frequency considered for imaging and characterisation (*i.e.* 3 MHz). This gives typical run time of 36 minutes for an FE model having 8.7×10^5 degrees of freedom, based on an Nvidia Quadro 600 GPU.

Two different average grain sizes, 0.2mm and 0.3mm, are considered in this paper. For each grain size, 50 random grain structures are simulated using the procedure described above where the shift parameter is set to be twice the mean grain size, giving grain structures similar to the one shown in Fig. 1(a). Figure 1(c) shows the grain size distribution calculated from 50 random grain structures for grain sizes 0.2mm and 0.3mm. The mean and standard deviation of the grain size distribution are 0.23mm and 0.11mm for the modelled grain size 0.2mm. For the modelled grain size 0.3mm, the mean and standard deviation are 0.34mm and 0.16mm. Cracks and holes

This article has been accepted for publication in a future issue of this journal, but has not been fully edited. Content may change prior to final publication. Citation information: DOI 10.1109/TUFFC.2019.2927439, IEEE Transactions on Ultrasonics, Ferroelectrics, and Frequency Control

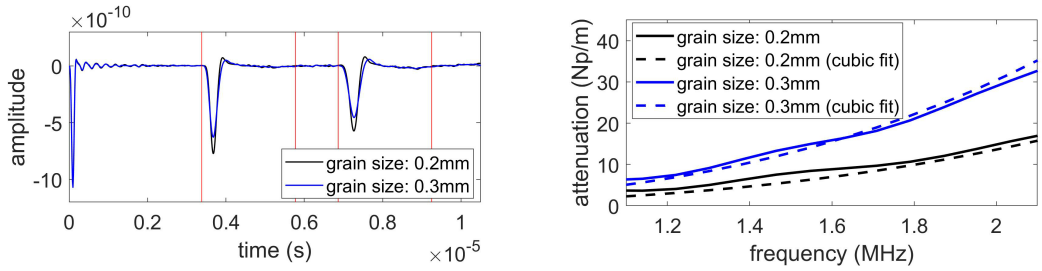

(a) (b)

Fig. 2. (a) Equivalent pulse-echo signals obtained by averaging the time-domain signals from 20 random grain structures, and (b) attenuation coefficients (dashed lines show the results of the cubic fit), for grain sizes 0.2mm and 0.3mm. Also shown in (a) are the FFT windows used for calculating the frequency spectra of the first and second back wall reflections.

of sizes 1mm, 2mm, and 3mm are chosen as target defects, and the random grain structures are used to simulate array data of the target defects. In addition, defect-free data for each of the grain structures are simulated and used to calculate the statistics of the grain noise distribution (termed the grains model hereafter).

B. Calculation of the equivalent ultrasonic velocity and attenuation coefficients

High resolution imaging algorithms such as the total focusing method (TFM) [4] work by synthetically focusing the ultrasonic beam at each pixel point. Focusing is achieved by calculation of delay laws for different array elements based on the propagation distance and the ultrasonic velocity [42]. In addition, amplitude reduction caused by attenuation should be compensated for when extracting scattering matrices from the array data. In this section, the ultrasonic velocity and frequency-dependent attenuation coefficients are calculated from simulated time domain data using the first and second back wall reflections from a defect-free sample [12]. For this purpose, 20 defect-free samples of 10mm depths are used in separate FE simulations for each grain size. The element size used in FE for calculations of the ultrasonic velocity and attenuation is 40μm, and this gives 5 elements per grain for the modelled grain size 0.2mm and 7.5 elements per grain for the grain size 0.3mm. Errors in attenuation and velocity obtained with similar settings (*i.e.* the ratio of the grain diameter to element size) were previously shown to be small (*i.e.* within 1.5% for attenuation and within 0.5% for velocity) compared to the use of smaller element sizes [34].

An equivalent pulse-echo signal is obtained by averaging signals recorded by all transmitter-receiver pairs of an array for all 20 simulations (see Fig. 2(a)). The ultrasonic velocity can be calculated based on the difference in the arrival times of the first and second back wall reflections. Note that averaging the time-domain signals of all transmitter-receiver pairs of an array is equivalent to using the array as a large unfocused monolithic transducer, and the effects of beam spreading are thus negligible [43]. Considering this, the attenuation coefficient is calculated by [12]

$$\alpha(\omega) = \frac{1}{2d}\ln\left|\frac{Q_1(\omega)}{Q_2(\omega)}\right|, \tag{1}$$

where Q_1 and Q_2 are frequency spectra of the first and second back wall reflections, respectively, and d=10mm is the depth of the sample. The attenuation coefficient results are shown in Fig. 2(b). A cubic line (dashed lines in Fig. 2(b)) is fitted to data within the usable bandwidth (*i.e.* between 1.1 MHz and 2.1 MHz) for each case to obtain attenuation coefficients within the whole frequency range considered. This follows from the relationship $\alpha \propto d^2k^3$ between the attenuation coefficient α, grain size d, and wavenumber $k = \omega/c$ in the Rayleigh regime assuming a 2D geometry [11]. The numerical attenuation of the mesh is not considered in this paper because its effect is small and negligible compared to attenuation caused by grain scattering. For example, the attenuation coefficient calculated by assigning uniform isotropic properties of stainless steel to all elements for the configuration shown in Fig. 1(b) is only 0.63 (unit: Np/m) at 2MHz, and this is an order of magnitude smaller than the attenuation corresponding to the grain size 0.2mm at the same frequency.

III. Imaging Results

In this section, the effect of grain scattering noise on defect imaging is investigated. The total focusing method (TFM) [4] is selected as the imaging algorithm here as it is one of the most widely adopted advanced imaging approaches in NDT and provides high resolution throughout the component [44]. For a point (x, z), its imaging amplitude is given by TFM as [4]

$$I(x,z) = \left|\sum_{u,v} g(u,v,t = \frac{\sqrt{(u-x)^2+z^2}+\sqrt{(v-x)^2+z^2}}{c})\right|, \tag{2}$$

where $g(u, v, t)$ denotes the signal measured by the transmitter-receiver pair where the locations of the transmitter and receiver elements are u and v, respectively (see Fig. 1(d)), and c is the ultrasonic velocity which can be calculated as described in Section II-B. TFM is applied to the simulated array data of a 1mm crack in a sample where the mean grain size is 0.2mm, and Figs. 3(a)-3(c) show the imaging results at 1-3MHz. Note that frequency filters with 50% half bandwidth are applied to the array data in these results, and "frequency" refers to the centre frequency in this paper. It is clearly seen that the TFM results progressively become dominated by grain

This article has been accepted for publication in a future issue of this journal, but has not been fully edited. Content may change prior to final publication. Citation information: DOI 10.1109/TUFFC.2019.2927439, IEEE Transactions on Ultrasonics, Ferroelectrics, and Frequency Control

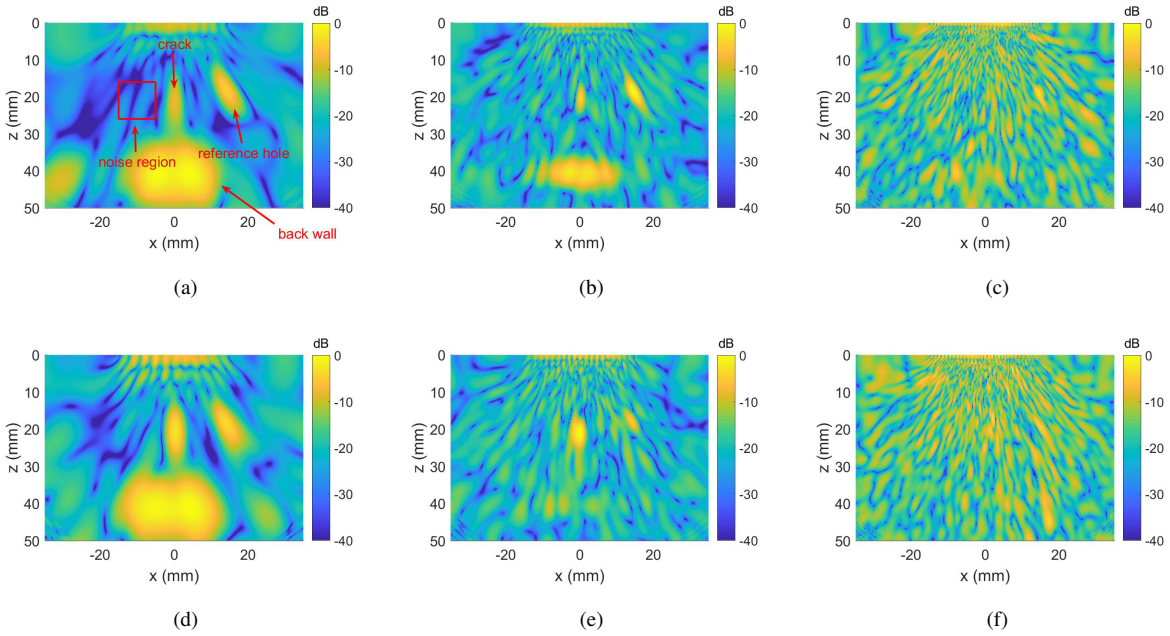

Fig. 3. TFM results of the target defects and grains. (a)-(c) a 1mm crack (the mean grain size is 0.2mm), and (d)-(f) a 3mm crack (the mean grain size is 0.3mm). The images show results obtained at 1 MHz (a and d), 2 MHz (b and e), and 3 MHz (c and f).

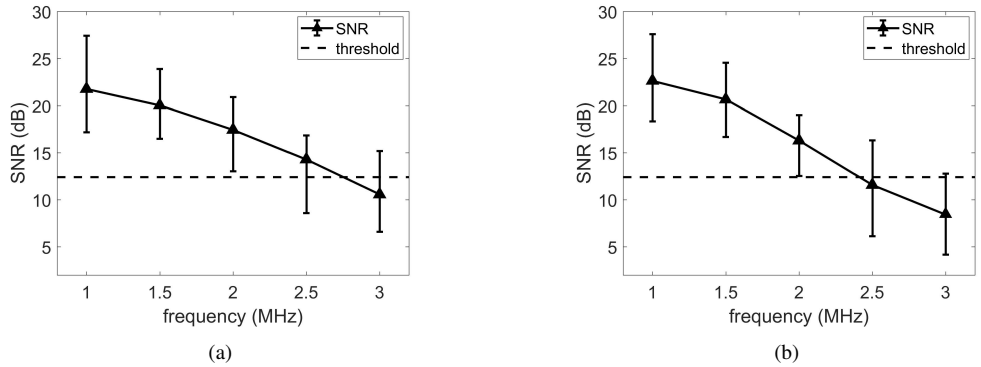

Fig. 4. SNR results of (a) 1mm cracks (the mean grain size is 0.2mm), and (b) 3mm cracks (the mean grain size is 0.3mm). The error bars show the maximum and minimum image SNRs, and triangles represent the median SNRs (calculated from 50 random grain structures).

noise as the frequency increases, and the defect indication is indistinguishable from the noise when the frequency is 3 MHz. Figures 3(d)-3(f) show the TFM results of a 3mm crack when the mean grain size of the sample is 0.3mm. Although a larger crack is imaged in these results, the defect is again undetectable when the frequency is 3 MHz due to the large grain size.

Quantitatively, the images obtained at different frequencies can be compared by their SNR values, which are defined as

$$\mathrm{SNR} = 20 \times \log_{10} \frac{I_d}{\mathrm{RMS}(n)}. \tag{3}$$

In Eq. (3), I_d is the maximum image amplitude of the defect, and $\mathrm{RMS}(n)$ denotes the root-mean-square amplitude of the noise, which is calculated within a 10mm$\times$10mm region on the left-hand-side of the defect and at a similar depth to the defect (*i.e.* the red box in Fig. 3(a)). Figures 4(a) and 4(b) show the SNR results extracted from images such as those shown in Fig. 3 for 1mm cracks (mean grain size: 0.2mm) and 3mm cracks (mean grain size: 0.3mm), respectively, in 0.5 MHz intervals between 1 MHz and 3 MHz. Each error bar shows the maximum and minimum image SNRs at a given frequency, and these results are obtained from 50 random grain structures used to simulate the array data. The SNR values decrease as the frequency increases, and hence, the detection performance of ultrasonic inspection is shown to be governed by grain noise. Note here that the ultrasonic velocity used in TFM calculations is 5582 m/s, and this is obtained from the equivalent pulse-echo signal corresponding to the grain size 0.2mm shown in Fig. 2(a). For grain sizes 0.2mm and 0.3mm, the variation in velocity for different Voronoi microstructures (20 random realisations are compared for each grain size) is small, and the velocity of the individual grains is within the range 5537-5612 m/s. The influence of the velocity variation on TFM results

This article has been accepted for publication in a future issue of this journal, but has not been fully edited. Content may change prior to final publication. Citation information: DOI 10.1109/TUFFC.2019.2927439, IEEE Transactions on Ultrasonics, Ferroelectrics, and Frequency Control

TABLE I
SNR COMPARISONS FOR 1MM CRACKS WITH THE MEAN GRAIN SIZE 0.2MM, CALCULATED FROM TFM IMAGES USING DIFFERENT VELOCITY VALUES.

Velocity (m/s)	Mean (dB)			Median (dB)			Standard deviation (dB)		
	1 MHz	2 MHz	3 MHz	1 MHz	2 MHz	3 MHz	1 MHz	2 MHz	3 MHz
5537	21.85	17.52	10.82	21.69	17.42	10.75	2.14	1.64	1.85
5582	21.85	17.48	10.73	21.78	17.43	10.57	2.14	1.62	1.82
5612	21.85	17.44	10.63	21.80	17.40	10.45	2.15	1.62	1.82

is also relatively small, and a comparison of the SNR results calculated using different velocity values (for the same case as in Fig. 4(a)) can be found in Table I. It can be seen from Table I that the difference in SNR is most significant at 3 MHz, with errors (relative to the results obtained with the velocity 5582 m/s) in mean, median and standard deviation within 0.1 dB, 0.18 dB, and 0.03 dB, respectively. In addition, SNR results obtained with the default element size (80μm) are compared to those obtained using a smaller element size (40μm) for 3mm cracks when the modelled grain size is 0.2mm. The difference in mean, median and standard deviation (calculated from 50 random grain structures as before) are found to be within 0.17 dB, 0.14 dB, and 0.04 dB, respectively, when the frequency is 3 MHz. This difference is considered to be small as it is comparable to the difference caused by the uncertainty in the ultrasonic velocity between different grain structures.

A detection threshold is needed to determine the existence of a defect. Figure 5 shows the distribution of the image amplitude within the noise region (see Fig. 3(a)) obtained from 50 TFM images of 1mm cracks (mean grain size and the frequency are 0.2mm and 3 MHz). As can be seen, noise amplitude in the image follows a Rayleigh distribution (red dashed line). Based on this observation, the detection threshold is set to be 12.4 dB (corresponding to the dashed lines in Figs. 4(a)-4(b)), and this gives a false call rate of 1/1000 for the considered image size in this paper. It can be seen from Fig. 4 that grain noise could potentially make both 1mm cracks (mean grain size: 0.2mm) and 3mm cracks (mean grain size: 0.3mm) undetectable when the frequency is 2.5 MHz and 3 MHz. For example, the probability of detection is below 50% for 1mm cracks when the frequency is 3 MHz (triangles in Fig. 4 represent the median SNR values). For 3mm cracks, their detection is shown to be fundamentally challenging with the probability of detection of only 4% when the frequency is 3 MHz because of the large grain size.

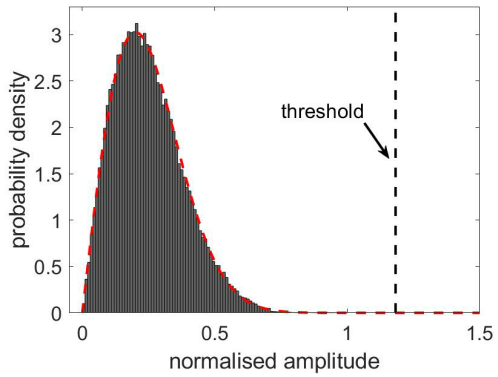

Fig. 5. Histogram plot of the noise amplitude obtained from 50 TFM images of 1mm cracks when the mean grain size of the sample is 0.2mm and the frequency is 3 MHz. Red dashed line shows a Rayleigh distribution fitted to the noise data, and black dashed line corresponds to the SNR detection threshold of 12.4 dB.

IV. DETECTION AND CHARACTERISATION OF DEFECTS USING THE SCATTERING MATRIX

A. The scattering matrix

Although the target defects can be detected when the frequency does not exceed 2 MHz as is shown in Figs. 3-4, defect characterisation from the image is difficult at these low frequencies due to the small defect size (relative to the wavelength). In this section, we consider using the scattering matrix for detection and characterisation of defects with the aim of improving the detection/characterisation accuracy. In a highly scattering medium, the scattering matrix can be defined as (assuming a 2D geometry as is shown in Fig. 1(d))

$$S(\theta_{\text{in}}, \theta_{\text{sc}}, \omega) = \frac{a_{\text{sc}}(\omega)}{a_{\text{in}}(\omega)} \sqrt{\frac{d_{\text{sc}}}{\lambda}} \exp\left(-\frac{i\omega d_{\text{sc}}}{c}\right) \exp\left[\alpha(\omega) d_{\text{sc}}\right], \tag{4}$$

where θ_{in}, θ_{sc} are the incident and scattering angles, a_{in}, a_{sc} are the amplitude of the plane incident wave at the defect and scattered wave measured at a distance d_{sc} from the defect, respectively, c is the ultrasonic velocity, α is the attenuation coefficient, λ is the wavelength, and ω is the angular frequency. The scattering matrix encodes the information about a defect in the form of the scattering coefficients for all incident and scattering angles. Although the scattering matrix is defined for different mode combinations, only the longitudinal-incident-longitudinal-scattering waves are considered in this paper. In addition, only the amplitude of the scattering matrix is extracted and used for characterisation because phase measurements are often associated with high uncertainty/large errors if the actual defect location is unknown [45]. The 5mm hole (see Fig. 1(b)) is introduced as the reference defect for purposes of amplitude normalisation in all simulations in this paper. More specifically, a separate ray-tracing approach is used to calculate the amplitude of the reference hole within the image when the incident pulse has the unity amplitude (the same ultrasonic velocity and attenuation coefficients as determined in Section II-B are used in the ray-tracing model). Before extracting the scattering matrix, the raw array data obtained from FE simulations are scaled so that the image amplitude

This article has been accepted for publication in a future issue of this journal, but has not been fully edited. Content may change prior to final publication. Citation information: DOI 10.1109/TUFFC.2019.2927439, IEEE Transactions on Ultrasonics, Ferroelectrics, and Frequency Control

of the reference hole is the same as that in the ray-tracing method. Note that the backwall is no longer an ideal reference defect for highly scattering materials because its amplitude can become very small and easily affected by noise. The 5mm hole is introduced closer to the array for this reason, and it is offset from the array centre to minimise its effects when extracting the scattering matrix of the target defect.

The main advantage of using the scattering matrix for characterisation is that defects remain distinguishable and characterisable in terms of their scattering matrices even for small defect sizes. For example, Figs. 6(a)-6(b) show the noise-free scattering matrices of a 3mm crack and a 3mm hole at 2 MHz, where the incident and scattering angle ranges are the same as those measurable from the configuration shown in Fig. 1(b). The ultrasonic wavelength of the modelled material is 2.8mm when the frequency is 2 MHz, meaning that both defects are comparable to the wavelength in size. For the scattering matrix of the crack, high amplitude values are found when $\theta_{\text{sc}} = -\theta_{\text{in}}$ (corresponding to the specular reflection), and the amplitude of the pulse-echo component of the scattering matrix (*i.e.* $\theta_{\text{sc}} = \theta_{\text{in}}$) decreases quickly when the incident angle θ_{in} moves away from 0° (which corresponds to the normal-incidence-normal-scattering case). On the other hand, the most significant feature of the scattering matrix of a hole is that the scattering coefficient is a constant value in pulse-echo (in fact, the scattering coefficient is only dependent on the difference between the incident and scattering angles and is the same in every diagonal component of the scattering matrix). It is found that within the measurable angular range, the maximum amplitude of the scattering matrix of a crack is higher than that of a hole which has the same size as the crack. For the size range considered in this paper, the difference in the scattering amplitude between cracks and holes is more significant for larger defects, and on average, the maximum scattering amplitude of a crack is 68% higher than that of a hole when the frequency is 2 MHz.

Figure 7 shows the scattering matrices of 3mm cracks (top row) and 3mm holes (bottom row) at 2 MHz, obtained from 4 different random realisations of grain structures of which the mean grain size is 0.2mm. As shown in Fig. 7, grain scattering introduces coherent noise to the measurement (*i.e.* it distorts the scattering matrix), and hence, degrades the characterisation performance. Although the scattering matrices of the cracks and holes still show different patterns, the effect of the grain scattering noise is also clearly observed in amplitude variations as well as a distortion of shape relative to the noise-free cases (Fig. 6). As a result, cracks can potentially be characterised as holes (or other volumetric defects such as ellipses) using classification approaches if the noisy scattering matrices are compared to a pre-computed defect database including only the noise-free scattering matrices [26]. As the grain size increases, the scattering matrices of the cracks and holes are affected by grain noise even more severely, and thus become more difficult to characterise.

B. Defect characterisation procedure

The key idea behind the defect characterisation approach adopted in this paper can be described using Bayes theorem [25], [46]:

$$P(\boldsymbol{p}|\boldsymbol{S}_n) = \frac{P(\boldsymbol{S}_n|\boldsymbol{p})P(\boldsymbol{p})}{P(\boldsymbol{S}_n)}. \tag{5}$$

In Eq. (5), $P(\boldsymbol{p}|\boldsymbol{S}_n)$ denotes the conditional probability of the defect parameter $\boldsymbol{p}$ (*e.g.* representing size and/or type of a defect) given the measurement of the noisy scattering matrix $\boldsymbol{S}_n$ (*e.g.* the ones shown in Fig. 7), and is the desired output of the defect characterisation process [25]. If we assume that the occurrence of different defects and scattering matrices are equally probable (*i.e.* $\boldsymbol{p}$ and $\boldsymbol{S}_n$ are uniformly distributed), Eq. (5) reduces to

$$P(\boldsymbol{p}|\boldsymbol{S}_n) = CP(\boldsymbol{S}_n|\boldsymbol{p}), \tag{6}$$

where C is a normalisation constant that can be calculated from $C = (\int P(\boldsymbol{S}_n|\boldsymbol{p})dp)^{-1}$. Note that prior knowledge about the defect parameter $\boldsymbol{p}$ can be readily incorporated into the Bayesian framework described above, in which case different normalisation constants need to be used for different defects [25]. In this paper, C is assumed to be a constant for simplicity.

Based on Eq. (6), it follows that the defect characterisation problem can be formulated as calculating $P(\boldsymbol{S}_n|\boldsymbol{p})$ for all possible defect parameters $\boldsymbol{p}$. The conditional probability $P(\boldsymbol{S}_n|\boldsymbol{p})$, *i.e.* the defect+grains model, describes the probability of measuring the noisy scattering matrix $\boldsymbol{S}_n$ from a defect with parameter $\boldsymbol{p}$. Being a statistical distribution by nature, the defect+grains model is the key component of the defect characterisation procedure adopted in this work.

The scattering matrix $\boldsymbol{S}_n$ ($\in \mathbb{R}^{N\times N}$ where N is the number of incident/scattering angles) normally has thousands of scattering coefficients corresponding to measurements from all transmitter-receiver pairs of an array. To avoid building a statistical distribution which has excessively large number of variables, $\boldsymbol{S}_n$ is transformed into a lower dimensional space by the use of principal component analysis (PCA) [47]. PCA is able to identify a small number of "directions" (termed the principal components) which are responsible for most of the variation in a data set. The PCA process effectively constructs a defect manifold [25] for modelled types of defects, and a large number of noise-free scattering matrices are needed for accurate reconstruction of the defect manifold (*i.e.* smooth surface for defects defined on 2D parameter spaces). Since the target defects considered in this paper are cracks and holes of different sizes, the noise-free data set can be obtained by sampling in both the defect size and aspect ratio (defined as the ratio between the width and length of a defect [26]) axes of the parameter space. Here the defect size is sampled in 0.05λ intervals between 0.05λ and 2λ, and aspect ratio is sampled in 0.1 intervals between 0 (cracks) and 1 (holes). Note that the target defects fall within the modelled size range of [0.05λ, 2λ] at all the frequencies considered in this paper. Although defect+grains modelling can be performed for each point on the defect manifold in principle, this is done only for the selected target defects in the current work because of the considerable computational time needed to run the FE models. The variance of the modelled scattering matrices in a principal component direction is equivalent to the corresponding eigenvalue of the covariance matrix of the

This article has been accepted for publication in a future issue of this journal, but has not been fully edited. Content may change prior to final publication. Citation information: DOI 10.1109/TUFFC.2019.2927439, IEEE Transactions on Ultrasonics, Ferroelectrics, and Frequency Control

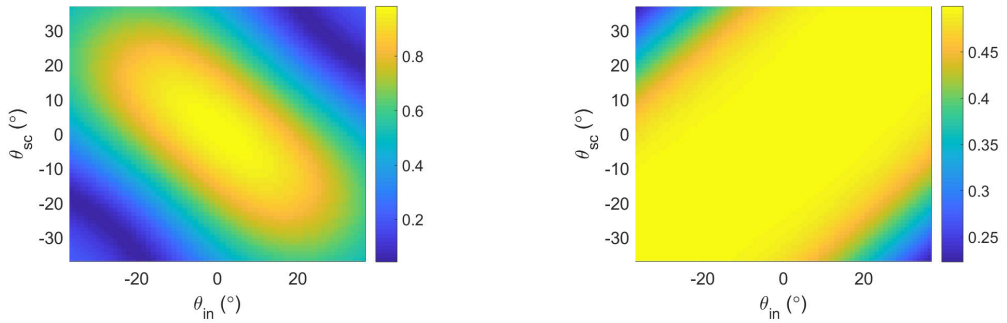

(a) (b)

Fig. 6. Noise-free scattering matrices of (a) a 3mm crack and (b) a 3mm hole, when the frequency is 2 MHz.

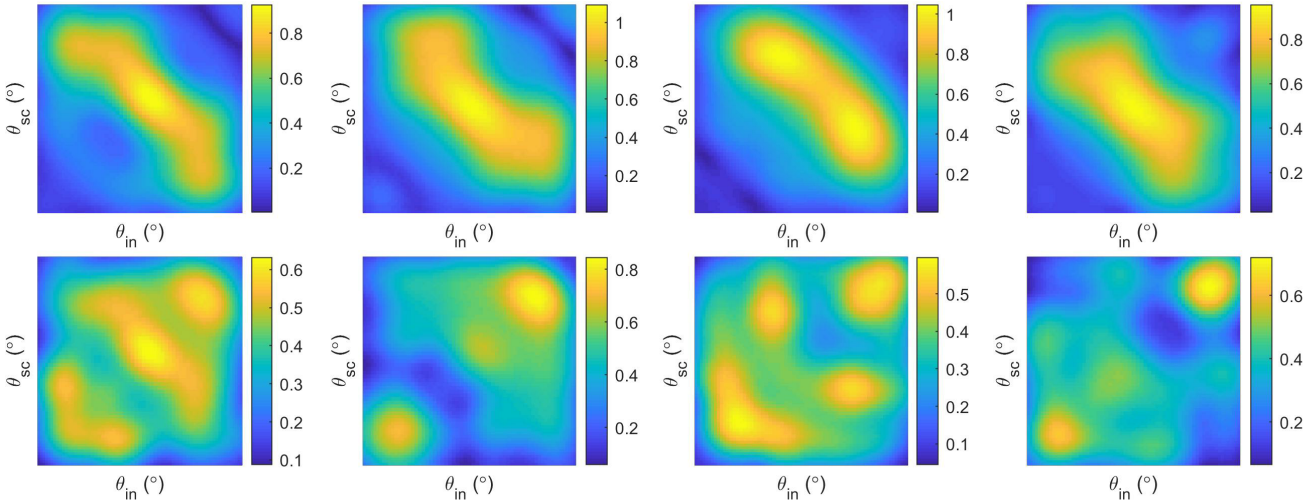

Fig. 7. Scattering matrices of 3mm cracks (top row) and 3mm holes (bottom row) at 2 MHz, obtained from 4 different grain structures of which the mean grain size is 0.2mm. Incident and scattering angle ranges of the scattering matrices are the same as those shown in Fig. 6.

database. Table II gives 10 largest eigenvalues obtained by the PCA process, from which it can be seen that the majority of information in a scattering matrix can indeed be encoded by a small number of the principal components. These principal components form the coordinate axes of a new space in which the defect+grains models are constructed, and this lower-dimensional space is termed the principal-component-space or PC-space hereafter.

The defect+grains model can now be written as $P(\boldsymbol{S}_n^{(\mathrm{pc})}|\boldsymbol{p})$ where $\boldsymbol{S}_n^{(\mathrm{pc})}$ represents the scattering matrix $\boldsymbol{S}_n$ in PC-space. In this paper, defect+grains models are assumed to follow a multivariate Gaussian distribution, which is given as [25]

$$P(\boldsymbol{S}_n^{(\mathrm{pc})}|\boldsymbol{p}) = \frac{1}{(2\pi)^{N_{PC}/2}|\boldsymbol{\Sigma}|^{1/2}} \times \exp\left(-\frac{1}{2}(\boldsymbol{S}_n^{(\mathrm{pc})}-\boldsymbol{\mu})^T\boldsymbol{\Sigma}^{-1}(\boldsymbol{S}_n^{(\mathrm{pc})}-\boldsymbol{\mu})\right), \tag{7}$$

where $\boldsymbol{\mu}$ and $\boldsymbol{\Sigma}$ denote the mean and covariance matrix, respectively, and can be estimated from the available training data by

$$\boldsymbol{\mu} = \sum_{i=i}^{N} \boldsymbol{S}_{n,i}^{(\mathrm{pc})}/N, \tag{8}$$

$$\boldsymbol{\Sigma} = \sum_{i=1}^{N} (\boldsymbol{S}_{n,i}^{(\mathrm{pc})}-\boldsymbol{\mu})(\boldsymbol{S}_{n,i}^{(\mathrm{pc})}-\boldsymbol{\mu})^T/(N-1). \tag{9}$$

In Eqs. (8)-(9), N=50 is the number of the noisy scattering matrices for each target defect, and $\boldsymbol{S}_{n,i}^{(\mathrm{pc})}$ denotes the i-th training data. Figure 8(a) shows defect+grains models of a 3mm crack (red contour lines) and a 3mm hole (blue contour lines) where the mean grain size is 0.2mm and the frequency is 2 MHz. The noise-free scattering matrices of the crack and hole are shown as the circles, and it can be seen that they are some distance away from the maximum probability points (corresponding to the mean noisy scattering matrices). The mean value of the grain noise in PC-space can be obtained as the difference between the maximum probability point and noise-free data point. Importantly, it can be seen that the defect+grains models of the crack and hole have different

This article has been accepted for publication in a future issue of this journal, but has not been fully edited. Content may change prior to final publication. Citation information: DOI 10.1109/TUFFC.2019.2927439, IEEE Transactions on Ultrasonics, Ferroelectrics, and Frequency Control

TABLE II
VARIANCE EXPLAINED BY (*i.e.* IMPORTANCE OF) THE FIRST 10 PRINCIPAL COMPONENT DIRECTIONS OF THE NOISE-FREE DEFECT DATABASE USED IN PCA.

PC number	1	2	3	4	5	6	7	8	9	10
Variance	48.07	11.94	1.23	0.37	0.14	0.07	0.06	0.03	0.02	0.01

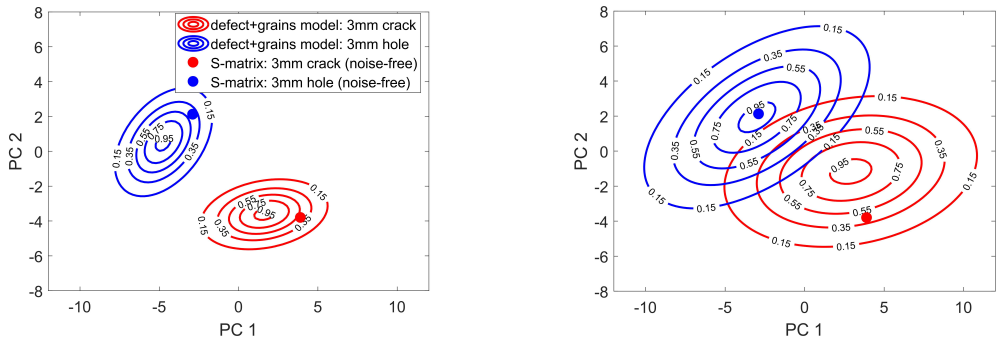

Fig. 8. Defect+grains models of a 3mm crack (red lines) and a 3mm hole (blue lines) for the mean grain size of (a) 0.2mm, and (b) 0.3mm. The frequency is 2 MHz, and the contour levels are normalised to 1 for each defect+grains model.

shapes (*e.g.* the 'orientations' of the contours that are determined by the covariance matrix in Eq. (9)), which means that defect+grains distribution is dependent on the defect parameter and should indeed be modelled separately for different defects. When the mean grain size becomes 0.3mm, the defect+grains models have significantly higher variance due to the increased grain noise and overlap with each other (see Fig. 8(b)). This explains why the scattering matrices measured from a crack and a hole can potentially become indistinguishable for certain grain structures.

C. An example case: detection/characterisation of a 1mm crack

The proposed approach is now used to characterise a 1mm crack in a sample where the mean grain size is 0.2mm. The inspection frequency is chosen to be 2.5 MHz, and Fig. 9(a) shows the TFM image of the defect (measurement configuration shown in Fig. 1(b) is adopted). The SNR value of the defect is calculated as 11.7 dB which is below the threshold of 12.4 dB. As a result, detection of the 1mm crack is challenging from the image. A scattering matrix is extracted from the defect location (indicated with an arrow in Fig. 9(a)), and it is then converted into the PC-space. The measurement is shown as the red circle in Fig. 9(b), where the contour plot represents the defect+grains model of a 1 mm crack. Given the defect+grains model and the measurement point in PC-space, the conditional probability $P(\boldsymbol{S}_n^{(\mathrm{pc})}|\boldsymbol{C}_1)$ can be calculated as 0.0065, where we used the notation $\boldsymbol{C}_1$ to denote the defect+grains model of the 1mm crack. Similarly, we can obtain $P(\boldsymbol{S}_n^{(\mathrm{pc})}|\boldsymbol{C}_2) = 4.4 \times 10^{-5}$ for the conditional probability with respect to a 2mm crack shown in Fig. 9(c). As can be seen, the conditional probability of observing the measurement is very low if the measurement is tested against a "wrong" defect+grains model. In Fig. 9(d), the contour plot represents the grains model, which shows the distribution of the scattering matrices measured from defect-free samples. The grains model is seen to be close to the measurement, and it gives conditional probability of the measurement that is higher than the individual defect+grains models of the cracks (*i.e.* $P(\boldsymbol{S}_n^{(\mathrm{pc})}|\boldsymbol{N}) = 0.0084$ where $\boldsymbol{N}$ denotes the grains model). This result can also explain why detection is inherently difficult from the image for this crack. The considered defect+grains models are plotted in Fig. 9(e) alongside the grains model, and it can be seen that the measurement lies within the overlapping region of the grains model and defect+grains models of the 1mm crack and holes of all sizes. Note that the defect+grains models are shown in 2D PC-space for purposes of visualisation and the probability of detection for the considered crack is only 63.3% in this case. For improved characterisation performance, a total of 7 PCs can be used for defect+grains modelling since the other PCs are less than 1% (relative to the first PC) in terms of the significance (*i.e.* variation of the database explained, see Table II). An excellent characterisation result is obtained by using 7 PCs as shown in Fig. 9(f) for the 1mm crack. However, it is noted that the example case shown here is taken from the training set, and actual characterisation performance is expected to drop for real measurements as will be discussed in the next section.

In summary, the proposed approach can be described algorithmically as follows:

- Step 1: Apply TFM or other imaging algorithms to array data and identify (from the image) regions of interest which could potentially contain defects.
- Step 2: Extract the scattering matrix $\boldsymbol{S}_n$ from a region of interest identified at Step 1, and convert it into the

This article has been accepted for publication in a future issue of this journal, but has not been fully edited. Content may change prior to final publication. Citation information: DOI 10.1109/TUFFC.2019.2927439, IEEE Transactions on Ultrasonics, Ferroelectrics, and Frequency Control

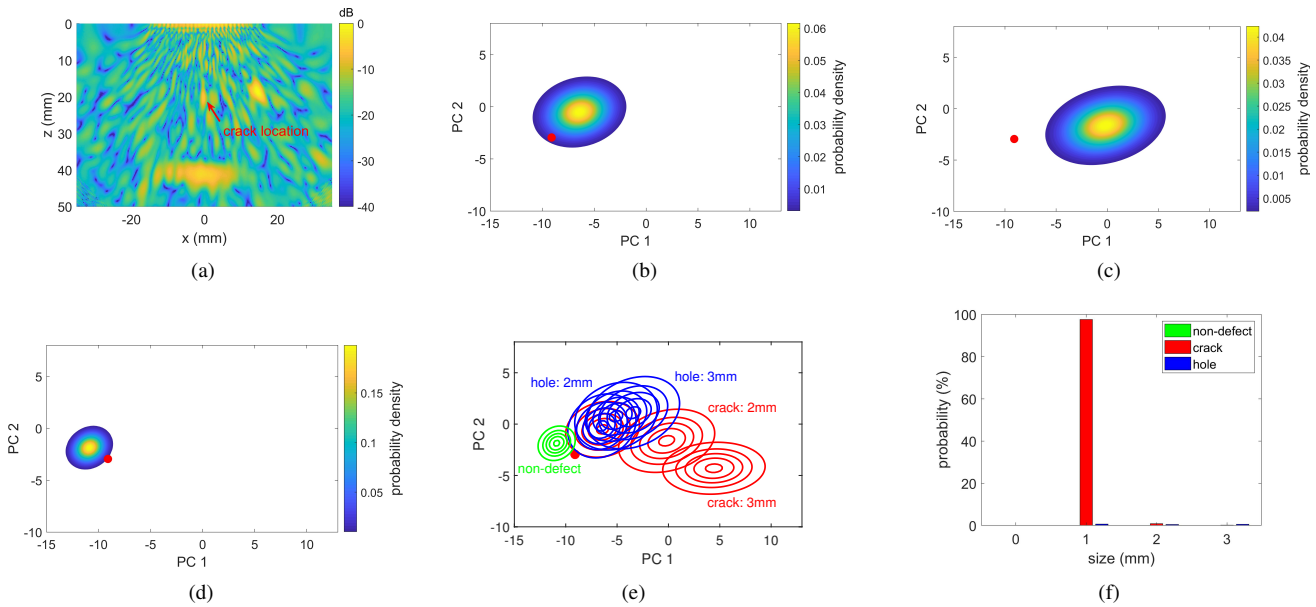

Fig. 9. Detection and characterisation of an example 1mm crack: (a) TFM image, (b) defect+grains model of a 1mm crack, (c) defect+grains model of a 2mm crack, (d) grains model, (e) all considered defect+grains models and the grains model, and (f) characterisation result obtained by using 7 PCs. The red circle in (b)-(e) represents the scattering matrix of the 1mm crack in PC-space, and the contour levels in (e) are the same as those shown in Fig. 8.

PC-space to obtain $\boldsymbol{S}_n^{(\mathrm{pc})}$.

- Step 3: For each defect+grains model in PC-space, calculate the conditional probability $P(\boldsymbol{S}_n^{(\mathrm{pc})}|\boldsymbol{p})$.
- Step 4: The defect characterisation result can be obtained as $P(\boldsymbol{p}|\boldsymbol{S}_n^{(\mathrm{pc})}) = CP(\boldsymbol{S}_n^{(\mathrm{pc})}|\boldsymbol{p})$, where $C = (\int P(\boldsymbol{S}_n|\boldsymbol{p})dp)^{-1}$.

D. Results

In this section, the performance of the proposed approach is studied by characterising test data which were not used for defect+grains modelling. For each target defect, scattering matrices are extracted from simulated array data based on 10 new grain structures, and the average characterisation results are shown in Figs. 10(a)-10(f) (the mean grain size modelled is 0.2mm and the frequency is 2 MHz). From the results of the cracks (Figs. 10(a)-10(c)), it is seen that cracks can be characterised accurately with higher confidence as the crack size increases. For the results of the holes (Fig. 10(d)-10(f)), however, uncertainty remains high for all defect sizes considered. This is because the defect+grains model of the 1mm crack overlaps with those of the holes (similar to the result shown in Fig. 9(e) which was obtained at 2.5 MHz). Also, there is a small probability that the 1mm hole could be left undetected (corresponding to the height of the green bar in Fig. 10(d)) while 1mm cracks are shown to achieve excellent probability of detection. This is believed to be related with the lower amplitude of the scattering matrices of the holes, when compared to cracks of the same size.

It is important to study the effect of frequency and grain size on detection/characterisation performance of the proposed approach. Here, we use probability of detection, classification accuracy, and sizing error to compare the results obtained at different frequencies (and for different grain sizes). Probability of detection gives the probability that a defect can be distinguished from noise, and is related to the detectability of a defect. Classification accuracy is defined as the probability that the defect type is correctly identified (*e.g.* sum of the probability of the red bars in Figs. 10(a)-10(c)), and the sizing error is given as the difference between the mean sizing result and the actual defect size. Figures 11(a)-11(c) show the characterisation results obtained for cracks of all sizes when the grain size is 0.2mm and 3mm cracks when the grain size is 0.3mm. It can be seen from Fig. 11(a) that probability of detection is near 100% for all the considered cases when the frequency is within 2 MHz. At 2.5 MHz and 3 MHz, the increased grain size (*i.e.* 0.3mm) has severely affected the detectability of 3mm cracks, and the probability of detection is lower than that of 1mm cracks (with the smaller grain size of 0.2mm). Similarly, increasing the frequency beyond 2 MHz is shown to result in lower classification accuracy (Fig. 11(b)) and larger sizing errors (Fig. 11(c)).

E. Comparison with the use of a general noise model

Compared to the defect characterisation approach proposed in [25], one of the main improvements achieved in the current work is that actual grain scattering noise is modelled and used for characterisation instead of making prior assumptions about the noise distribution. Noise was previously modelled to have the same distribution as that of two-dimensional Gaussian random rough surfaces [48], and the same parameters used for describing a rough surface in 2D were adopted as parameters characterising this so-called general coherent noise model [25]. Although the covariance matrix $\boldsymbol{\Sigma}$ of the Gaussian distribution (see Eq. (7)) can potentially be made close to the true value by optimising parameters of the general coherent noise model [25], the distribution of the defect+grains models obtained

This article has been accepted for publication in a future issue of this journal, but has not been fully edited. Content may change prior to final publication. Citation information: DOI 10.1109/TUFFC.2019.2927439, IEEE Transactions on Ultrasonics, Ferroelectrics, and Frequency Control

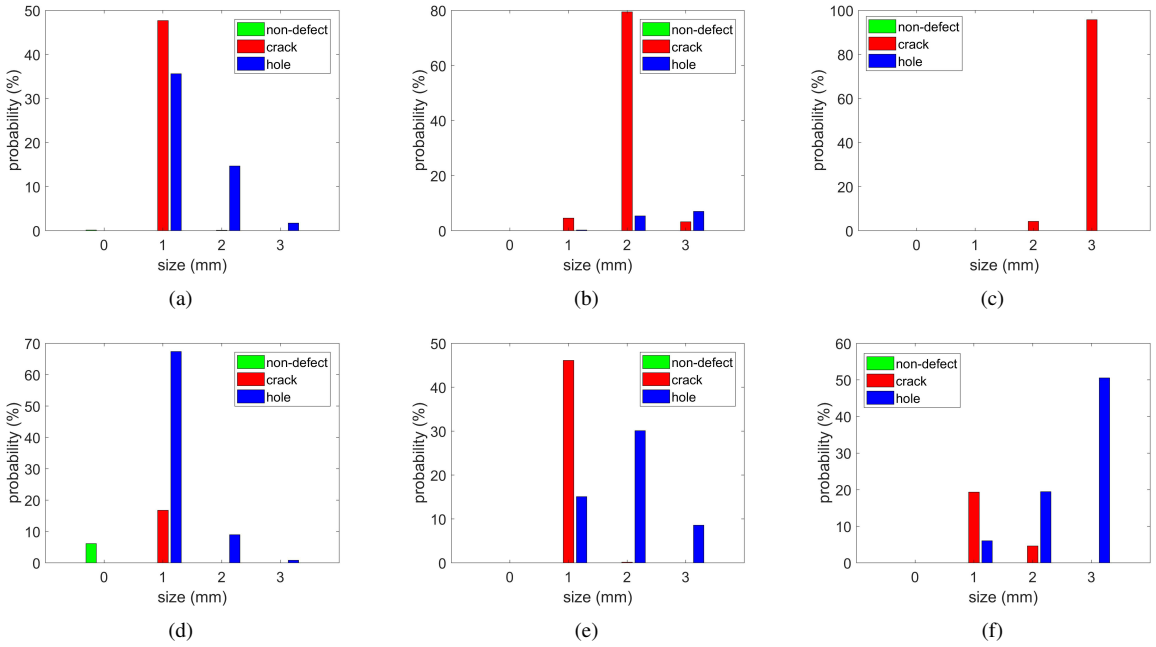

Fig. 10. Average characterisation results of different defects when the frequency is 2 MHz and the mean grain size is 0.2mm, where (a) 1mm cracks, (b) 2mm cracks, (c) 3mm cracks, (d) 1mm holes, (e) 2mm holes, and (f) 3mm holes.

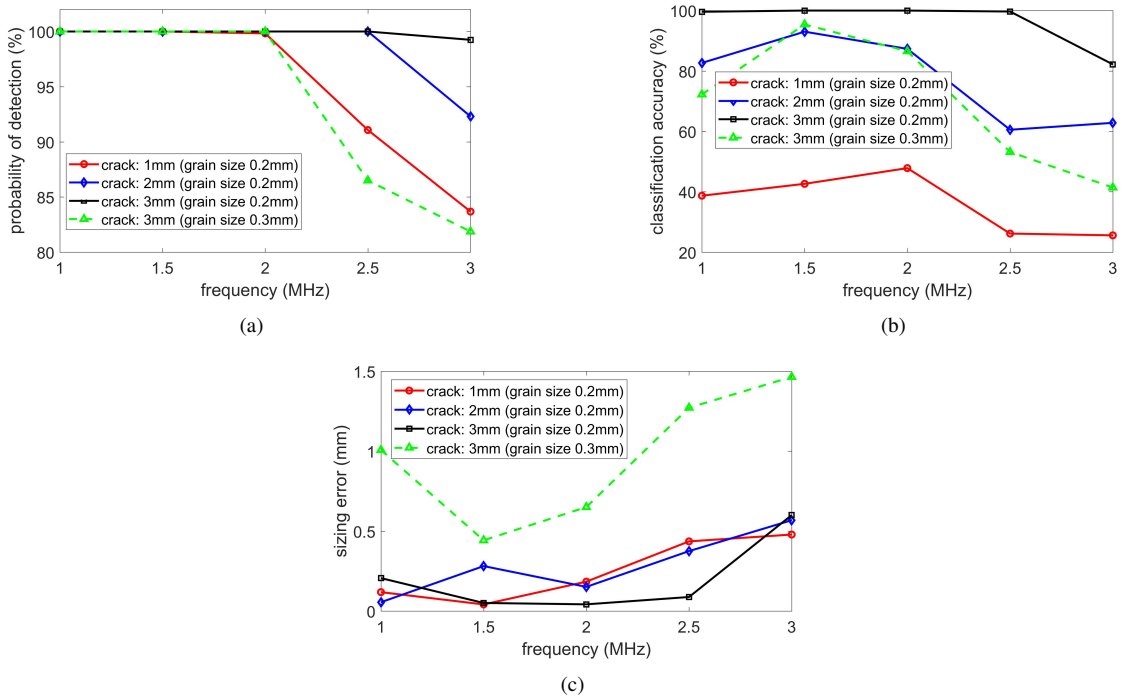

Fig. 11. Characterisation results of the cracks at different frequencies, where (a) probability of detection, (b) classification accuracy, and (c) sizing error.

with the zero-mean assumption would always be centred at the noise-free data (*i.e.* $\boldsymbol{\mu}$ equals to the noise-free scattering matrix in Eq. (7), but this is shown not to be the case for grain scattering noise in Fig. 8). Inaccurate grain noise modelling could lead to poor characterisation results. Figure 12(a) shows the characterisation result of the non-defect case which is obtained from 10 new grain structures as before (the mean grain size is 0.2mm). The actual grains and defect+grains models are used in Fig. 12(a), and the considered frequency is 3 MHz as the effect of grain scattering noise is most significant at this high frequency. We can see that false alarms do appear due to the high noise level but the probability of the correct category (*i.e.* 'non-defect') is still dominant (*i.e.* near 80%). Figure 12(b) shows the result obtained with the general

This article has been accepted for publication in a future issue of this journal, but has not been fully edited. Content may change prior to final publication. Citation information: DOI 10.1109/TUFFC.2019.2927439, IEEE Transactions on Ultrasonics, Ferroelectrics, and Frequency Control

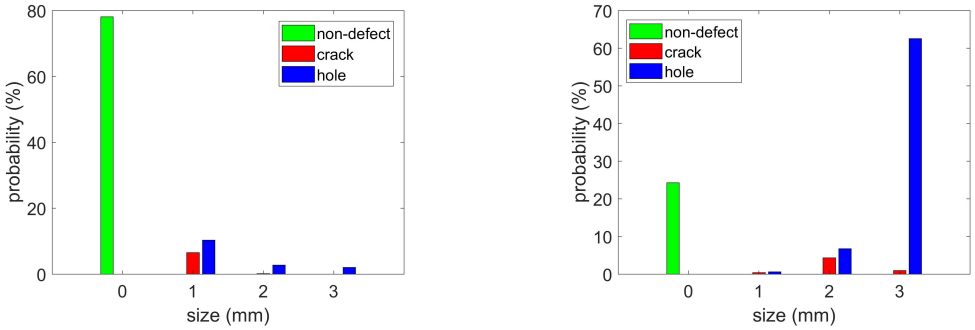

Fig. 12. Characterisation results of non-defect cases when the mean grain size is 0.2mm and the frequency is 3 MHz, where (a) the actual grains and defect+grains models and (b) the general coherent noise model [25] are used for characterisation.

coherent noise model [25]. It can be seen that the use of inaccurate noise model has yielded poor characterisation result with the false alarm rate of 75.7%, although the parameters of the general coherent noise model are carefully selected using the maximum-likelihood estimation method [45]. The mean value of the scattering matrix is zero if there is no defect according to the zero-mean noise assumption. However, in practice, the measured scattering matrix contains contributions from grain scattering even when there is no defect, and as a result, such measurements are often characterised as defects using the general coherent noise model as can be seen in Fig. 12(b).

F. Discussions

From the results shown in Fig. 11, we find that the classification accuracy and sizing accuracy of a defect are not necessarily the same. For example, 3mm cracks with the larger grain size of 0.3mm (green dashed lines in Fig. 11) can still achieve excellent classification accuracy at 1.5 MHz and 2 MHz (*i.e.* above 80%), but the sizing results are poor (*i.e.* close to or larger than 0.5mm). A similar scenario can be found in Fig. 9(e) — the defect+grains model of the 3mm crack is well separated from those of holes which could result in excellent classification results for 3mm cracks, while there is still uncertainty in sizing due to the overlap between defect+grains models of 2mm and 3mm cracks. On the other hand, although the classification accuracy is consistently below 50% for 1mm cracks, the sizing errors are small at frequencies between 1 MHz and 2 MHz. This suggests that different defects can achieve different levels of characterisation in practice, such as detectable, classifiable (*i.e.* only the defect type can be determined), and characterisable (*i.e.* both the type and size of the defect can be determined).

The defect+grains model introduced in this paper describes the variability of the measurement due to noise, and hence, contains information about the achievable characterisation performance. The critical observation is that characterisation uncertainty arises when there is overlapping between two or more defect+grains models, as is explained in Section IV-C. The amount of overlapping between two statistical distributions can be quantified by Bhattacharyya coefficient, which is defined as [49]

$$B(f,g) = \int \sqrt{f(x)g(x)}dx, \tag{10}$$

where $f(x)$ and $g(x)$ are probability density functions of variable x and satisfy $\int f(x)dx = \int g(x)dx = 1$. It follows from Cauchy-Schwarz inequality [50] that $0 \leq B(f,g) \leq \int f(x)dx \cdot \int g(x)dx = 1$. The Bhattacharyya coefficient is 0 if f and g do not overlap and is 1 if f is equal to g. In other cases, the Bhattacharyya coefficient is within the range (0,1), and higher values indicate more severe overlapping of two distributions. Based on the Bhattacharyya coefficient, we define the detectability index (d-index) of a crack as

$$d(i) = 1 - B(\boldsymbol{C}_i, \boldsymbol{N}), \tag{11}$$

where as in Section IV-C, $\boldsymbol{C}_i$ denotes the defect+grains model of a crack with size i (unit: mm) and $\boldsymbol{N}$ represents the grains model. The d-index of different cracks for both grain sizes and different frequencies are given in Table III, and the results are shown to be highly correlated with the actual probability of detection (see Fig. 11(a)). For example, when the frequency is 3 MHz, the d-index of 3mm cracks (grain size: 0.3mm) is smaller than that of 1mm cracks (grain size: 0.2mm), and this is reflected as the lower probability of detection. We also find that the d-index of 1mm cracks decreases quickly as frequency increases when the grain size is 0.3mm, and is near 0 at 3 MHz. This indicates that detection of small cracks is fundamentally challenging when the frequency is high.

Similarly, the classification index (c-index) can be defined for a crack as

$$c(i) = 1 - \max\left\{B(\boldsymbol{C}_i, \boldsymbol{H}_j)\right\}, j = 1, 2, 3, \tag{12}$$

where $\boldsymbol{H}_j$ denotes the defect+grains model of a hole with size j. As can be seen from Eq. (12), c-index quantifies the degree of overlapping between the defect+grains model of a crack and those of the holes which causes misclassification of the defect type. The c-index values of the cracks are summarised in Table IV, and once again, good agreement is found between the c-index values and actual classification accuracy shown in Fig. 11(b). For example, the c-index of 1mm cracks is consistently

This article has been accepted for publication in a future issue of this journal, but has not been fully edited. Content may change prior to final publication. Citation information: DOI 10.1109/TUFFC.2019.2927439, IEEE Transactions on Ultrasonics, Ferroelectrics, and Frequency Control

TABLE III
D-INDEX (SEE EQ. (11)) OF CRACKS AT DIFFERENT FREQUENCIES.

Grain	1 MHz			1.5 MHz			2 MHz			2.5 MHz			3 MHz		
	1mm	2mm	3mm	1mm	2mm	3mm	1mm	2mm	3mm	1mm	2mm	3mm	1mm	2mm	3mm
0.2mm	1.00	1.00	1.00	1.00	1.00	1.00	0.96	1.00	1.00	0.86	1.00	1.00	0.56	0.92	0.99
0.3mm	1.00	1.00	1.00	0.87	0.98	1.00	0.55	0.91	0.96	0.23	0.61	0.82	0.04	0.13	0.27

TABLE IV
C-INDEX (SEE EQ. (12)) OF CRACKS AT DIFFERENT FREQUENCIES.

Grain	1 MHz			1.5 MHz			2 MHz			2.5 MHz			3 MHz		
	1mm	2mm	3mm	1mm	2mm	3mm	1mm	2mm	3mm	1mm	2mm	3mm	1mm	2mm	3mm
0.2mm	0.21	0.67	0.95	0.24	0.67	0.99	0.25	0.77	0.99	0.17	0.65	0.98	0.14	0.52	0.87
0.3mm	0.09	0.58	0.86	0.13	0.45	0.82	0.20	0.25	0.65	0.12	0.27	0.56	0.05	0.08	0.18

TABLE V
S-INDEX (SEE EQ. (13)) OF CRACKS AT DIFFERENT FREQUENCIES.

Grain	1 MHz			1.5 MHz			2 MHz			2.5 MHz			3 MHz		
	1mm	2mm	3mm	1mm	2mm	3mm	1mm	2mm	3mm	1mm	2mm	3mm	1mm	2mm	3mm
0.2mm	0.65	0.62	0.62	0.54	0.68	0.88	0.26	0.77	0.84	0.30	0.65	0.71	0.14	0.45	0.45
0.3mm	0.45	0.55	0.55	0.32	0.32	0.55	0.24	0.25	0.31	0.12	0.20	0.20	0.05	0.06	0.06

small at all frequencies and the classification accuracy was shown to be below 50%. The c-index of 2mm and 3mm cracks remain high within the frequency range [1 MHz, 2 MHz] when the grain size is 0.2mm, and they are shown to be classified with high accuracy (*i.e.* over 80%). Inconsistencies are found, for example, the relatively large c-index of the 2mm crack (grain size: 0.2mm) and its low classification accuracy (*i.e.* 60.5%) at 2.5 MHz. However, this is believed to be related with the small number of test data, and is expected to improve as more data are used for testing. In fact, the Bhattacharyya coefficient defined in Eq. (10) is related to a lower bound of the achievable classification performance [51]. We find that the classification accuracy is satisfactory when the c-index is above 0.7, with which the Bayes error rate (*i.e.* misclassification rate achievable by using the Bayes classifier) has an upper bound of 15%. The classification accuracy of 1mm and 2mm cracks is expected to be poor when the grain size is 0.3mm due to their low c-index values, but 3mm cracks can still be classified accurately at frequencies between 1 MHz and 2 MHz (this can be confirmed from Fig. 11(b)).

Lastly, the sizing index (s-index) can be defined for a crack as

$$s(i) = 1 - \max\left\{B(\boldsymbol{C}_i, \boldsymbol{C}_j), B(\boldsymbol{C}_i, \boldsymbol{H}_j)\right\}, j \neq i. \qquad (13)$$

The s-index results of the cracks are given in Table V, which can be used to compare and evaluate the sizing accuracy of a crack in different measurement scenarios. When the grain size is 0.2mm, some large s-index values are found (*e.g.* 2 MHz for 2mm crack, as well as 1.5 MHz and 2 MHz for 3mm crack), all of which are shown to have small sizing errors in Fig. 11(c). When the grain size is 0.3mm, the s-index value is small (*i.e.* below 0.6) for all crack sizes and frequencies, suggesting that sizing of the cracks has become more challenging due to the increased grain size.

In order to study the effect of the element size used in FE forward modelling on characterisation, the same 50 grain structures previously used for defect+grains modelling are used to simulate the array data of 3mm cracks and 3mm holes with a smaller element size of 40μm (the studied grain size is 0.2mm). The defect+grains models obtained with different element sizes are compared in Table VI using the Bhattacharyya coefficient, where $\boldsymbol{C}_3'$ and $\boldsymbol{H}_3'$ denote the defect+grains models of 3mm cracks and 3mm holes obtained with the smaller element size. The first two rows of Table VI confirm that defect+grains models calculated using the default element size (80μm) are indeed in good match with those calculated with smaller elements since the similarity measured by the Bhattacharyya coefficient is over 0.9 at all frequencies (and over 0.95 at 1-2 MHz). The third and fourth rows of Table VI suggest that the amount of overlapping (between defect+grains models of 3mm cracks and 3mm holes) calculated with the default element size is also in good agreement with that obtained using smaller elements. As a result, the selection of the element size (80μm) is considered to be sufficient for the purpose of this paper. However, it is also expected that the use of smaller elements and 3D FE models could further improve the accuracy of forward modelling, and future work will aim to understand the limitation of 2D modelling for characterisation of real defects within polycrystalline materials.

This article has been accepted for publication in a future issue of this journal, but has not been fully edited. Content may change prior to final publication. Citation information: DOI 10.1109/TUFFC.2019.2927439, IEEE Transactions on Ultrasonics, Ferroelectrics, and Frequency Control

TABLE VI
THE BHATTACHARYYA COEFFICIENT BETWEEN DEFECT+GRAINS MODELS OBTAINED WITH DIFFERENT ELEMENT SIZES ($\boldsymbol{C}_3'$ AND $\boldsymbol{H}_3'$ DENOTE THE DEFECT+GRAINS MODELS OF 3MM CRACKS AND 3MM HOLES OBTAINED WITH THE ELEMENT SIZE 40μM.)

Bhattacharyya coefficient	1 MHz	1.5 MHz	2 MHz	2.5 MHz	3 MHz
$B(\boldsymbol{C}_3, \boldsymbol{C}_3')$	0.98	0.96	0.95	0.95	0.94
$B(\boldsymbol{H}_3, \boldsymbol{H}_3')$	0.97	0.98	0.96	0.92	0.91
$B(\boldsymbol{C}_3, \boldsymbol{H}_3)$	0.06	0.01	0.01	0.02	0.13
$B(\boldsymbol{C}_3', \boldsymbol{H}_3')$	0.04	4.3×10^{-3}	4.1×10^{-3}	0.01	0.12

The proposed defect+grains modelling approach shows that forward modelling based on *a priori* knowledge about the grain size distribution within a material and anisotropic material properties can provide important information that is useful for accurate detection and characterisation of defects. In addition, the achievable detection/characterisation accuracy can reliably be predicted by quantifying the amount of overlap between different defect+grains models. This information can be used in different aspects of ultrasonic NDT, including array optimisation (*e.g.* selecting the optimum frequency and/or bandwidth), inversion framework optimisation (*e.g.* selecting optimal resolution/interval of defect parameters), and selection of the measurement channels and/or wave modes in ultrasonic data fusion (*i.e.* only include data which are expected to improve the detection/characterisation performance). Moreover, the proposed approach can be extended to characterise different types of defects, such as surface-breaking cracks and branched cracks, since they can also be described by a small number of parameters [25].

V. CONCLUSIONS

In this paper, the statistics of the defect and noise scattering matrices in noisy materials are explored based on repeated forward simulations. Firstly, a grain structure is simulated as a Voronoi diagram that can be obtained from randomly shifted nodes (corresponding to the vertexes of a grain). Secondly, an FE model is prepared by introducing a target defect into the simulated grain structure, and the array data is computed by running FE simulations. Thirdly, the scattering matrix of the defect is extracted from the simulated array data, and is used as the basis for the proposed characterisation approach.

The defect+grains model describes the variability of the defect scattering matrix for a given grain size and frequency, and can be constructed using scattering data obtained from multiple realisations of the grain structure. Given any measurement, the probability that the scattering matrix is measured from a specific defect+grains model can be calculated, and it is shown that this probability is proportional to the probability of the considered defect+grains model given the measurement. Hence, the defect characterisation problem can be formulated by constructing a defect+grains model for each target defect and calculating the conditional probability of them given the measurement. This means that if the measurement is within the overlapping region of several defect+grains models, its characterisation result will have a probability distribution over the corresponding defect parameters, *i.e.*, there is characterisation uncertainty.

Because the defect+grains models contains all the information that is required by characterisation, the achievable characterisation performance can be evaluated by quantifying the amount of overlapping between different defect+grains models. The detectability index, classification index, and sizing index are defined based on the Bhattacharyya coefficient and as their names suggest, are related with different levels of defect characterisation. By calculating these index values (and also by comparing with the characterisation results obtained from the test data), it is shown that the achievable characterisation accuracy is different for different defects. The actual characterisation performance is shown to be predictable using the different index values defined in this paper, and as a result, these index values provide important information for inspection of highly scattering materials. However, it is worth pointing out that the results presented in this paper should not be used to make predictions about other combinations of the defect size, grain size, and the wavelength. Instead, defect+grains modelling should always be performed based on actual parameter values.

In order for the proposed defect+grains modelling approach to be adopted in practical industrial applications, better understanding of the material under inspection is necessary, including not only the average grain size and grain size variation, but also anisotropic material properties and information about the grain shape (*e.g.* equiaxed or elongated). These can be used in FE simulations to obtain multiple realisations of the defect and noise data for purposes of statistical modelling. Alternatively, the grain scattering data (with and without the presence of a defect) can be measured experimentally from different regions of a test specimen or specimens which are known to have similar grain structures. Also, it is important to note that defect+grains modelling should ideally be performed separately for defects at different locations (relative to the array), since the effect of grain scattering noise is also different (in particular, at different depths). Lastly, it is noted that the accuracy of the FE modelling adopted in this paper has the potential for further improvements by using more comprehensive 3D models. The shapes of real grains and defects are intrinsically 3D, and hence, 3D modelling of grain and defect scattering is expected to improve the reliability of defect characterisation.

ACKNOWLEDGMENT

The project leading to this application has received funding from the European Union's Horizon 2020 research and innovation programme under grant agreement No 755500.

REFERENCES

[1] J. D. Achenbach, "Quantitative nondestructive evaluation," *Int. J. Solids Struct.*, vol. 37, no. 1-2, pp. 13–27, 2000.

[2] T. Kundu, *Ultrasonic Nondestructive Evaluation: Engineering and Biological Material Characterization*. Boca Raton, FL: CRC Press, 2004.

[3] S. J. Song, H. J. Shin, and Y. H. Jang, "Development of an ultrasonic phased array system for nondestructive tests of nuclear power plant components," *Nucl. Eng. Design*, vol. 214, no. 1-2, pp. 151–161, 2002.

[4] C. Holmes, B. W. Drinkwater, and P. D. Wilcox, "Post-processing of the full matrix of ultrasonic transmit-receive array data for nondestructive evaluation," *NDT E Int.*, vol. 38, no. 8, pp. 701–711, 2005.

[5] N. Pörtzgen, D. Gisolf, and G. Blacquiere, "Inverse wave field extrapolation: A different NDI approach to imaging defects," *IEEE Trans. Ultrason. Ferroelectr. Freq. Control*, vol. 54, no. 1, pp. 118–127, 2007.

[6] A. J. Hunter, B. W. Drinkwater, and P. D. Wilcox, "The wavenumber algorithm for full-matrix imaging using an ultrasonic array," *IEEE Trans. Ultrason. Ferroelectr. Freq. Control*, vol. 55, no. 11, pp. 2450–2462, 2008.

[7] J. Blitz and G. Simpson, *Ultrasonic Methods of Non-Destructive Testing*, 1st ed. London, UK: Chapman & Hall, 1996.

[8] B. Shakibi, F. Honarvar, M. D. Moles, J. Caldwell, and A. N. Sinclair, "Resolution enhancement of ultrasonic defect signals for crack sizing," *NDT E Int.*, vol. 52, pp. 37–50, Nov. 2012.

[9] J. Zhang, B. W. Drinkwater, and P. D. Wilcox, "The use of ultrasonic arrays to characterize crack-like defects," *J. Nondestruct. Eval.*, vol. 29, no. 4, pp. 222–232, 2010.

[10] L. J. Cunningham, A. J. Mulholland, K. M. Tant, A. Gachagan, G. Harvey, and C. Bird, "The detection of flaws in austenitic welds using the decomposition of the time-reversal operator," *Proc. R. Soc. A*, vol. 472, no. 2188, p. 20150500, 2016.

[11] A. Van Pamel, P. B. Nagy, and M. J. Lowe, "On the dimensionality of elastic wave scattering within heterogeneous media," *J. Acoust. Soc. Am.*, vol. 140, no. 6, pp. 4360–4366, 2016.

[12] H. A. Bloxham, A. Velichko, and P. D. Wilcox, "Establishing the limits of validity of the superposition of experimental and analytical ultrasonic responses for simulating imaging data," *IEEE Trans. Ultrason. Ferroelectr. Freq. Control*, vol. 66, no. 1, pp. 101–108, 2019.

[13] F. J. Margetan, R. B. Thompson, and I. Yalda-Mooshabad, "Backscattered microstructural noise in ultrasonic toneburst inspections," *J. Nondestruct. Eval.*, vol. 13, no. 3, pp. 111–136, 1994.

[14] C. Fan, M. Caleap, M. Pan, and B. W. Drinkwater, "A comparison between ultrasonic array beamforming and super resolution imaging algorithms for non-destructive evaluation," *Ultrasonics*, vol. 54, no. 7, pp. 1842–1850, 2014.

[15] V. L. Newhouse, N. M. Bilgutay, J. Saniie, and E. S. Furgason, "Flaw-to-grain echo enhancement by split-spectrum processing," *Ultrasonics*, vol. 20, no. 2, pp. 59–68, 1982.

[16] V. Matz, R. Smid, S. Starman, and M. Kreidl, "Signal-to-noise ratio enhancement based on wavelet filtering in ultrasonic testing," *Ultrasonics*, vol. 49, no. 8, pp. 752–759, 2009.

[17] A. Praveen, K. Vijayarekha, S. T. Abraham, and B. Venkatraman, "Signal quality enhancement using higher order wavelets for ultrasonic TOFD signals from austenitic stainless steel welds," *Ultrasonics*, vol. 53, no. 7, pp. 1288–1292, 2013.

[18] J. Kim, L. Udpa, and S. Udpa, "Multi-stage adaptive noise cancellation for ultrasonic NDE," *NDT E Int.*, vol. 34, no. 5, pp. 319–328, 2001.

[19] M. A. Izquierdo, M. G. Hernandez, O. Graullera, and L. G. Ullate, "Time-frequency Wiener filtering for structural noise reduction," *Ultrasonics*, vol. 40, no. 1-8, pp. 259–261, 2002.

[20] A. Aubry and A. Derode, "Detection and imaging in a random medium: A matrix method to overcome multiple scattering and aberration," *J. Appl. Phys.*, vol. 106, no. 4, p. 044903, 2009.

[21] C. Prada, S. Manneville, D. Spoliansky, and M. Fink, "Decomposition of the time reversal operator: Detection and selective focusing on two scatterers," *J. Acoust. Soc. Am.*, vol. 99, no. 4, pp. 2067–2076, 1996.

[22] S. Shahjahan, A. Aubry, F. Rupin, B. Chassignole, and A. Derode, "A random matrix approach to detect defects in a strongly scattering polycrystal: How the memory effect can help overcome multiple scattering," *Appl. Phys. Lett.*, vol. 104, no. 23, p. 234105, 2014.

[23] F. Xie, L. Moreau, Y. Zhang, and E. Larose, "A Bayesian approach for high resolution imaging of small changes in multiple scattering media," *Ultrasonics*, vol. 64, pp. 106–114, Jan. 2016.

[24] N. Brierley, T. Tippetts, and P. Cawley, "Data fusion for automated non-destructive inspection," *Proc. R. Soc. A*, vol. 470, no. 2167, p. 20140167, 2014.

[25] A. Velichko, L. Bai, and B. W. Drinkwater, "Ultrasonic defect characterisation using parametric-manifold mapping," *Proc. R. Soc. A*, vol. 473, no. 2202, p. 20170056, 2017.

[26] L. Bai, A. Velichko, and B. W. Drinkwater, "Characterization of defects using ultrasonic arrays: A dynamic classifier approach," *IEEE Trans. Ultrason. Ferroelectr. Freq. Control*, vol. 62, no. 12, pp. 2146–2160, 2015.

[27] J. Zhang, B. W. Drinkwater, and P. D. Wilcox, "Defect characterization using an ultrasonic array to measure the scattering coefficient matrix," *IEEE Trans. Ultrason. Ferroelectr. Freq. Control*, vol. 55, no. 10, pp. 2254–2265, 2008.

[28] A. Velichko and P. D. Wilcox, "Reversible back-propagation imaging algorithm for postprocessing of ultrasonic array data," *IEEE Trans. Ultrason. Ferroelectr. Freq. Control*, vol. 56, no. 11, pp. 2492–2503, 2009.

[29] M. Kitahara, K. Nakahata, and S. Hirose, "Elastodynamic inversion for shape reconstruction and type classification of flaws," *Wave Motion*, vol. 36, no. 4, pp. 443–455, 2002.

[30] M. Brigante, "Numerical algorithm for defect reconstruction in elastic media with a circular ultrasonic scanning," *Eng. Anal. Bound. Elem.*, vol. 37, no. 3, pp. 551–557, 2013.

[31] D. Colton, J. Coyle, and P. Monk, "Recent developments in inverse acoustic scattering theory," *SIAM Rev.*, vol. 42, no. 3, pp. 369–414, 2000.

[32] S. Shahjahan, F. Rupin, A. Aubry, B. Chassignole, T. Fouquet, and A. Derode, "Comparison between experimental and 2-D numerical studies of multiple scattering in Inconel600® by means of array probes," *Ultrasonics*, vol. 54, no. 1, pp. 358–367, 2014.

[33] A. Van Pamel, G. Sha, S. I. Rokhlin, and M. J. Lowe, "Finite-element modelling of elastic wave propagation and scattering within heterogeneous media," *Proc. R. Soc. A*, vol. 473, no. 2197, p. 20160738, 2017.

[34] A. Van Pamel, C. R. Brett, P. Huthwaite, and M. J. Lowe, "Finite element modelling of elastic wave scattering within a polycrystalline material in two and three dimensions," *J. Acoust. Soc. Am.*, vol. 138, no. 4, pp. 2326–2336, 2015.

[35] G. Ghoshal and J. A. Turner, "Numerical model of longitudinal wave scattering in polycrystals," *IEEE Trans. Ultrason. Ferroelectr. Freq. Control*, vol. 56, no. 7, pp. 1419–1428, 2009.

[36] R. D. Cook, D. S. Malkus, M. E. Plesha, and R. J. Witt, *Concepts and Applications of Finite Element Analysis*. New York, NY: Wiley, 2007.

[37] F. Aurenhammer, "Voronoi diagrams-a survey of a fundamental geometric data structure," *ACM Comput. Surv.*, vol. 23, no. 3, pp. 345–405, 1991.

[38] S. Ahmed and R. B. Thompson, "Propagation of elastic waves in equiaxed stainless-steel polycrystals with aligned [001] axes," *J. Acoust. Soc. Am.*, vol. 99, no. 4, pp. 2086–2096, 1996.

[39] D. S. Kupperman and K. J. Reimann, "Effect of shear-wave polarization on defect detection in stainless steel weld metal," *Ultrasonics*, vol. 16, no. 1, pp. 21–27, 1978.

[40] L. W. Schmerr, *Fundamentals of Ultrasonic Nondestructive Evaluation-A Modeling Approach*. New York, NY: Plenum Press, 1998.

[41] P. Huthwaite, "Accelerated finite element elastodynamic simulations using the GPU," *J. Comput. Phys.*, vol. 257, pp. 687–707, Jan. 2014.

[42] M. Sutcliffe, M. Weston, B. Dutton, P. Charlton, and K. Donne, "Real-time full matrix capture for ultrasonic non-destructive testing with acceleration of post-processing through graphic hardware," *NDT E Int.*, vol. 51, pp. 16–23, Oct. 2012.

[43] H. A. Bloxham, A. Velichko, and P. D. Wilcox, "Combining simulated and experimental data to simulate ultrasonic array data from defects in materials with high structural noise," *IEEE Trans. Ultrason. Ferroelectr. Freq. Control*, vol. 63, no. 12, pp. 2198–2206, 2016.

[44] M. Sutcliffe, P. Charlton, and M. Weston, "Multiple virtual source aperture imaging for non-destructive testing," *Insight*, vol. 56, no. 2, pp. 75–81, 2014.

[45] L. Bai, A. Velichko, and B. W. Drinkwater, "Ultrasonic defect characterisation-use of amplitude, phase, and frequency information," *J. Acoust. Soc. Am.*, vol. 143, no. 1, pp. 349–360, 2018.

[46] T. Hastie, R. Tibshirani, and J. Friedman, *The Elements of Statistical Learning*, 2nd ed. New York, NY: Springer-Verlag, 2009.

[47] I. T. Jolliffe, *Principal Component Analysis*, 2nd ed. New York, NY: Springer-Verlag, 2002.

[48] F. Shi, W. Choi, M. J. Lowe, E. A. Skelton, and R. V. Craster, "The validity of Kirchhoff theory for scattering of elastic waves from rough surfaces," *Proc. R. Soc. A*, vol. 471, no. 2178, p. 20140977, 2015.

[49] T. Kailath, "The divergence and Bhattacharyya distance measures in signal selection," *IEEE Trans. Commun. Technol.*, vol. 15, no. 1, pp. 52–60, 1967.
[50] M. Abramowitz and I. A. Stegun, *Handbook of Mathematical Functions with Formulas, Graphs, and Mathematical Tables*. New York, NY: Dover, 1972.
[51] P. A. Devijver and J. Kittler, *Pattern Recognition: A Statistical Approach*. London, UK: Prentice hall, 1982.